Ultrasonics 99 (2019) 105948

Contents lists available at ScienceDirect

Ultrasonics

journal homepage: www.elsevier.com/locate/ultras

Automatic mode extraction of ultrasonic guided waves using synchrosqueezed wavelet transform

Zhenli Liu[a], Kailiang Xu[a,*], Dan Li[a], Dean Ta[a,b,*], Weiqi Wang[a]

[a] Department of Electronic Engineering, Fudan University, 200433 Shanghai, China
[b] State Key Laboratory of ASIC and System, Fudan University, 200433 Shanghai, China

ARTICLE INFO

Keywords:
Ultrasonic guided waves
Mode separation
Synchrosqueezed wavelet transform

ABSTRACT

Multimodal and dispersive characteristics of ultrasonic guided waves (GWs) cause the wave-packet overlapping in time domain and frequency domain, which challenges the signal interpretation. In this study, we propose an automatic method for individual mode extraction. The inversible synchrosqueezed wavelet transform (SWT) is employed to obtain the high-resolution time-frequency representation (TFR) of the GW signal. Then, two image processing steps, *i.e.*, watershed transform and region growing, are used to process the TFR distributions and extract the TFR trajectory of each individual component. After the TFR segmentation, the individual modes are reconstructed by using the inverse SWT. The algorithm performance is investigated by synthesized multimodal signals. The results show that the reconstructed individual modes are consistent with the original ones. The experimental results measured in a bovine tibia plate and a steel plate are further employed to testify the proposed algorithm. Results suggest that the presented study provides a robust tool for processing multimodal ultrasonic GW signals.

1. Introduction

Due to its sensitivity to waveguide geometry and material elasticity, the ultrasonic guided wave (GW) has been used as an effective tool in material characterization [1], nondestructive testing (NDT) [2], structural health monitoring [3] and biomedical application, *e.g.*, long bone evaluation [4]. However, as a result of multimodal dispersion, GW signals are typically measured as a combination of multiple wave packets, which leads to difficulties in signal interpretation and parameter estimation.

In response to the challenge, a great attention has been paid to selectively excite the individual guided mode [5]. For instance, according to Snell's law, angle wedges have been employed to selectively excite guided modes [6]. Recently, a dual-element transducer excitation [7] and a dispersive coded excitation [8] have been proposed to dominantly generate the selected guided modes. However, such selective excitation methods cannot ensure a full suppression of the rest modes in received signals. It is of necessity to develop signal processing methods to separate the overlapped modes and extract the dispersion curves for waveguide characterization.

One of the classical methods is two-dimensional Fourier transform (2DFT), which distinguishes different modes by projecting the temporal-spatial signals into the frequency-wavenumber domain [9]. In order to improve the extraction of dispersion curves, a singular vector decomposition (SVD) based method has been developed with a multi-emitter and multi-receiver transducer array [10], and successfully applied to GW signals in the long bone [11]. Considering the sparsity of the dispersion curves, sparse wavenumber analysis [12,13] and compressed sensing [14,15] have been proposed. Combining the sparse regularization with SVD-based techniques, Xu et al. [16] advanced a sparse SVD method to enable the extraction of high-resolution dispersion curves. Okumura et al. [17] introduced a model-based adaptive array signal processing method for dispersion curves determination. As an alternative solution to 2DFT, Radon transform (RT) [18] and high-resolution RT [19] have been applied for GW signal processing. The high-resolution RT enables a better resolution than 2DFT [20]. However, the classical and high-resolution RT methods could be unsuitable for wideband GW signal processing [21]. To overcome the limitation, Xu et al. [22] extended the classical RT with a nonlinear dispersive projection strategy, and developed the dispersive RT method. The aforementioned methods are designed for signals recorded at several positions, and may not be applicable for processing a single multimodal GW signal. To separate multimodal GW components in one signal, the dispersion compensation method [23] and Vold-Kalman filter [24] have been used. The methods show a good performance in mode recognition but both require the prior knowledge of dispersion characteristics.

* Corresponding authors at: Department of Electronic Engineering, Fudan University, 200433 Shanghai, China (D. Ta).
E-mail addresses: xukl@fudan.edu.cn (K. Xu), tda@fudan.edu.cn (D. Ta).

https://doi.org/10.1016/j.ultras.2019.105948
Received 14 January 2019; Received in revised form 19 June 2019; Accepted 19 June 2019
Available online 20 June 2019
0041-624X/

Another possible way to process GW signals is the time-frequency (TF) analysis method, such as short-time Fourier transform (STFT), continuous wavelet transform and Wigner-Ville distribution (WVD) [25]. Recently, a new TF analysis method named synchrosqueezed wavelet transform (SWT) has been proposed to enhance the TF resolution in comparison to the classical TF analysis [26]. The idea of SWT, inspired from wavelet transform and the relocation method, was originally developed by Daubechies [27] for multicomponent speech signal isolation. It reassigns the scale variable of wavelet transform into the frequency variable, after which the time-scale energy of the signal can be compressed in the time-frequency domain. SWT has been used in speech recognition [27], climate studies [28], geophysics [29], structural damage detecting [30] and image processing [31]. In addition, Bause et al. [32] have applied a joint SWT and ridge-extraction method for ultrasonic GW signal decomposition and group delay estimation. Ikram et al. [33] have used SWT to extract the TF characteristics of GW signals propagating through a complex integrated circuit and realized integrated circuit package health inspection.

As different modes distribute along the different dispersion curves which across different sets of time and frequency atoms, the image segmentation methods can be used to extract them in time-frequency domain. Watershed transform is able to segment an image into distinct regions by regarding it as a landscape [34]. The region growing algorithm could gather pixels by comparing the similarity between the adjacent pixels and seed regions [35]. In the study, we propose a mode separation and reconstruction method, which combines the SWT, watershed transform and region growing, to achieve an automatic mode extraction of GW signals. The method was testified by using the GWs in plate-like waveguide, *i.e.*, synthetic multimodal signals, experimental signals measured from a steel plate [23] and a bovine tibia plate.

The paper is organized as follows. In Section 2, the simulation and experimental setup are illustrated. The SWT-based mode separation method is introduced in Section 3. After the results and discussion given in Sections 4 and 5, the conclusion can be found in Section 6.

2. Simulation and experimental setup

The simulation and experiment were carried out on a 4-mm-thick bovine tibia plate, whose material parameters are listed in Table 1 [36]. With the known dispersion curve of a given mode, the temporal GW signal $g(t)$ measured at distance x_0 can be synthesized by using the dispersion propagation function $H(\omega)$ [37]:

$$g(t) = \frac{1}{2\pi}\int_{-\infty}^{\infty} S(\omega)H(\omega)e^{j\omega t}d\omega \tag{1a}$$

$$H(\omega) = e^{-jk(\omega)x_0} \tag{1b}$$

where $S(\omega)$ represents the spectrum of the excitation. According to the GW theory, the wavenumber $k(\omega)$ of a given mode is a function of angular frequency ω. In this paper, three Lamb modes, A1, S1 and S2, were synthesized separately and mixed together as the simulated signal. The experiment was conducted using the ultrasonic axial transmission method with a pitch-and-catch distance of 70 mm. A pair of unfocused ultrasonic transducers (ValpeyFisher), both with the central frequency of 0.40 MHz, were employed to excite and receive the GWs. Ultrasound gel was used to ensure the coupling between the transducers and the bone plate.

Table 1
Material parameters of the bovine bone plate.

Parameters	Value
Density ρ	1.85 g/cm3
Thickness h	4 mm
Shear velocity V_t	1.98 km/s
Longitudinal velocity V_l	3.55 km/s

Apart from the signal measured in bovine tibia, a multimode signal measured in an 1 mm steel plate was also used as experimental data, which comes from Ref. [23] with a source-receiver distance of 460 mm.

3. Methods

Fig. 1 presents a schematic diagram of the mode separation and reconstruction algorithm. First, SWT was employed to obtain the TFR of the multimodal GWs. Then, image segmentation methods, including watershed transform [34] and region growing [35], were introduced to identify the individual components in the TF domain. Finally, we reconstructed the individual modes of the input signal based on the segmented SWT representation using inverse SWT. The algorithm was tested by simulated data at varying signal-to-noise ratios (SNRs) as well as the *in vitro* experimental signals.

The algorithm was developed under MATLAB programming environment. SWT and inverse SWT were performed using the functions “wsst” and “iwsst” in Wavelet Toolbox. The function “watershed” included in MATLAB Image Processing Toolbox was utilized to obtain the watershed results. Please refer to [38] for mathematically rigorous definitions of the watershed algorithm. The region growing algorithm will be detailed in Section 3.2.2.

3.1. SWT representation

SWT enables the optimization of the TFR of signals by reassigning the scale variable of wavelet transform to the frequency variable. For a temporal signal $f(t)$, the wavelet transform can be described as [39]:

$$WT(a, b) = \int_{-\infty}^{\infty} f(t)\frac{1}{\sqrt{|a|}}\varphi\left(\frac{t-b}{a}\right)dt \tag{2}$$

The function $\frac{1}{\sqrt{|a|}}\varphi\left(\frac{t-b}{a}\right)$, referred to as a daughter wavelet, is the mother wavelet function $\varphi(t)$ dilated by a scale a and shifted in time by a translational value b. Variable a is used to control the time duration of daughter wavelets. According to Eq. (2), we can obtain a wavelet projection of the signal onto a set of daughter wavelets.

SWT is developed to convert the time-scale plane of wavelet transform to the time-frequency plane. We define the reference instantaneous frequency function as $\omega(a, b) = \frac{\frac{\partial}{\partial b}WT(a,b)}{2\pi i WT(a,b)}$ [39]. The SWT of the signal $f(t)$ can be calculated by [39]:

$$SWT(\xi, b) = \int_{\{a\neq 0, WT(a,b)\neq 0\}} WT(a, b)\delta(\omega(a, b) - \xi)\frac{da}{a} \tag{3}$$

where ξ is the frequency variable. The δ function is known as the Dirac Delta function, which equals to zero everywhere except the origin.

3.2. SWT representation segmentation

Each individual mode can be distinguished as a set of local maxima along its individual time-frequency ridge. The time and frequency coordinates of the local maxima correspond to the arrival times and central frequencies. Let Q_k represent the energy maximum of the kth mode along the time-frequency ridge. The following segmentation procedure can be performed using Q_k (k = 1, 2, …, K) as input parameters, where K represents the number of the modes. For the purpose of restraining oversegmentation, a preprocessing step, including Gaussian filtering, morphological opening and closing [40], is applied to the SWT representation.

3.2.1. Watershed algorithm

Watershed transform was further applied to segment the SWT representation. The concept underlying watershed transform comes from the imagination of an immersion analogy process: basins of a landscape are gradually immersed by water starting at the local minima and ending at points where water coming from different basins encounters

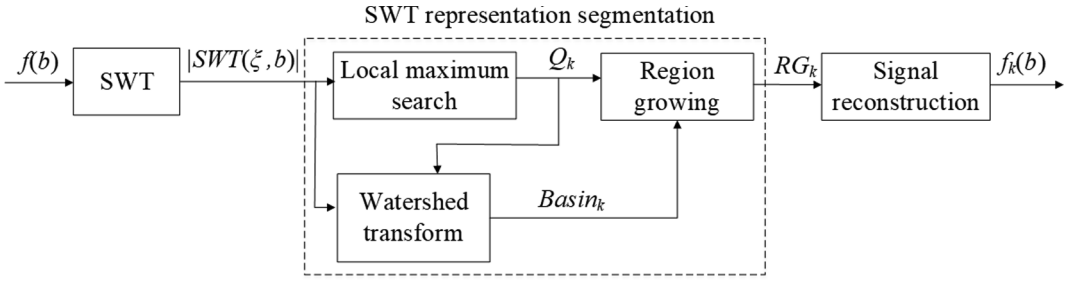

Fig. 1. Schematic diagram of the proposed algorithm.

each other [34]. Afterwards, the boundary lines among these basins, also called watersheds, can divide the landscape into several parts. The energy peaks (Q_1, Q_2, …, Q_K) are converted into the local minima by inversing the absolute value of the SWT ($|SWT(\xi, b)|$), and used as the initial seeds of watershed transform. The algorithm of watershed transform is realized by a recursive procedure, which can be learned in [38].

After watershed transform, the SWT representation is divided into K regions, each of which is denoted by $Basin_k$. Each region can be further divided into two different areas: one consists of the TF energy of the corresponding guided mode, while the other can be seen as the background. The next step for SWT representation segmentation is to refine the boundary lines by region growing.

3.2.2. Region growing

The region growing method is then introduced to grow regions by grouping pixels with their neighbors according to a predefined threshold criteria. We define RG_k^l as the points in the region experiencing l times growth starting at Q_k. Let $Neigh[RG_k^l]$ represent the neighboring points of RG_k^l. Let θ denote the threshold selected according to the SNR. The region growing algorithm for the kth mode can be realized as follows:

(1) Initialize $l = 1$, and $RG_k^l = \{Q_k\}$.
(2) Obtain RG_k^l from RG_k^{l-1}:
For each point $P \in (Neigh[RG_k^{l-1}] \bigcap Basin_k)$, if the value of P is smaller than θ, incorporate P into RG_k^{l-1} to form RG_k^l.
(3) Repeat (2) to update RG_k^l, until there is no P satisfying the condition in (2).

Finally, the region of each individual mode in the SWT representation is obtained. Let RG_k represent the points in the final segmented region associated with the Q_k.

3.3. Signal reconstruction

After SWT representation segmentation, we can reconstruct the individual component by inversing the SWT representation $SWT(\xi, b)$ in each segmented region. Considering the fact that the kth reconstructed mode $f_k(b)$ is real, we finally have [39],

$$f_k(b) = \mathrm{Re}\left(\frac{2}{c_\varphi}\int_0^\infty SWT_k(\xi, b)d\xi\right) \tag{4a}$$

$$SWT_k(\xi, b) = \begin{cases} SWT(\xi, b), & \text{when } (\xi, b) \in RG_k. \\ 0, & \text{else.} \end{cases} \tag{4b}$$

where the coefficient c_φ is given by [39]:

$$c_\varphi = \int_0^\infty \int_{-\infty}^\infty \varphi(t)e^{-2\pi i\xi t}dt\frac{d\xi}{\xi} \tag{4c}$$

4. Results

4.1. Simulated signals of bovine bone plate

The SWT representation and the segmentation results of the noise-free synthetic signal are depicted in Fig. 2a. The SWT representation of the GW signal concentrates along the theoretical dispersion curves. The color maps the signal energy on the TF sampling points with high in red and low in blue. The aforementioned watershed transform and region growing method are then employed to extract the TFR of each individual mode. The black solid lines correspond to the extracted boundaries of the TF region of individual components. Fig. 2b shows the STFT spectrogram of the synthetic signal. The frequency resolutions of both methods are then compared by using the normalized TF energy intensity functions of the signal at 100 μs. As can be seen in Fig. 2c, the main lobe widths obtained by the STFT and SWT methods are 0.07 MHz and 0.01 MHz, respectively, which indicates that the SWT method can achieve a higher frequency resolution than the classical SWT method.

According to Eq. (4), the temporal signals of simulated modes can be reconstructed with the segmented region. As shown in Fig. 3, the reconstructed and original data are noted in red lines and blue[1] lines, respectively. The reconstructed signals of A1, S1, S2 and the multimode are all in good agreement with their original signals. To quantitatively evaluate the quality of reconstruction signals, the correlation coefficient is used to measure the similarity between the reconstructed signal $Rec(t)$ and the original signal $Ori(t)$.

$$Corr(Rec, Ori) = \frac{Cov(Rec, Ori)}{\sigma_{Rec}\sigma_{Ori}} \tag{5}$$

where $Cov(Rec, Ori)$ is the covariance between $Rec(t)$ and $Ori(t)$, and σ_{Rec} and σ_{Ori} represent the standard deviation of the two signals. With such a definition, the correlation coefficients can be calculated at 0.999, 0.995, 0.993 and 0.999 for A1, S1, S2 and the multimode, respectively.

To test the robustness of the proposed algorithm, some Gaussian random noise was added to the simulated signal with different SNRs, which can be calculated by,

$$SNR = 10\log_{10}\frac{p_{sig}}{p_{noi}} \tag{6}$$

where p_{noi} and p_{sig} are the mean power of the noise and signal, respectively. Considering that the duration of the simulated signal is shorter than the total data acquisition time, the leading and trailing zeros are truncated for computing the accurate signal mean power. When SNR = 0 dB, the original multimodal signal is heavily polluted by noise, as given in Fig. 4d, but the guided modes A1, S1 and S2 can be still separated and reconstructed in a good agreement with their original signals, as shown in Fig. 4a–c. The correlation coefficients between the reconstructed and original signals are 0.984, 0.973, 0.959 and 0.980 for A1, S1, S2 and the multimode, respectively. Compared

[1] For interpretation of color in Fig. 3, the reader is referred to the web version of this article.

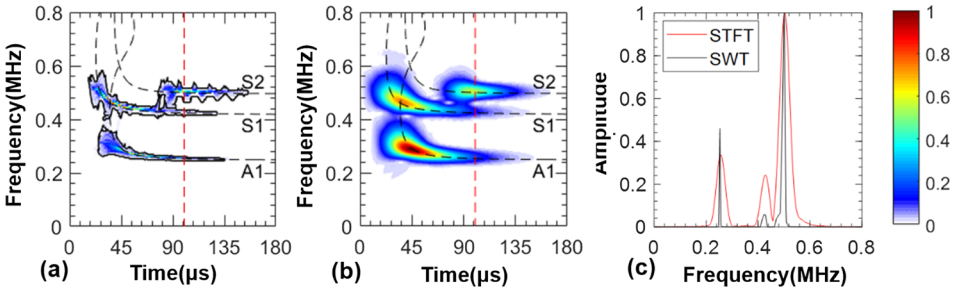

Fig. 2. Noise-free synthetic signal: (a) SWT representation segmentation, (b) STFT spectrogram, (c) Comparison of the TFR amplitude functions obtained at 100 μs. The 100 μs time point is indicated by red dashed vertical lines in (a) and (b). (For interpretation of the references to color in this figure legend, the reader is referred to the web version of this article.)

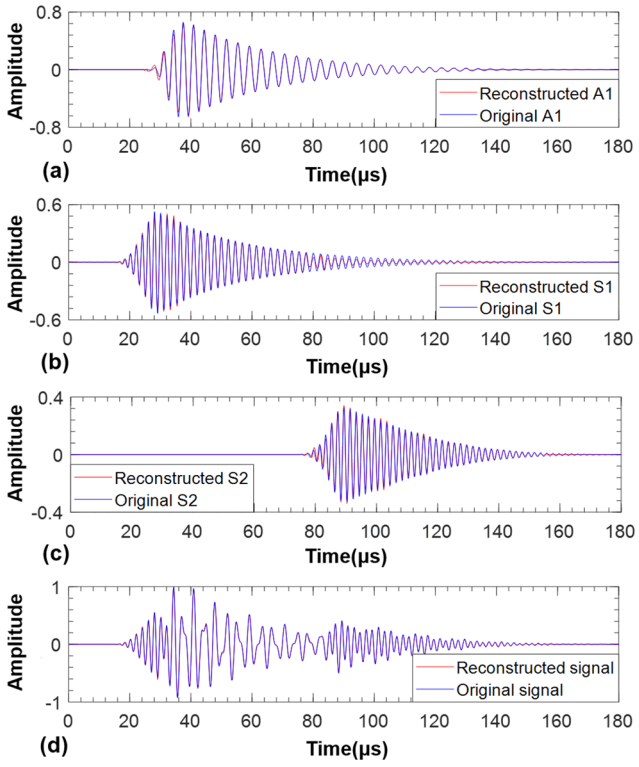

Fig. 3. Reconstructed synthetic signals (SNR = ∞): (a) A1 mode; (b) S1 mode; (c) S2 mode; (d) multimode.

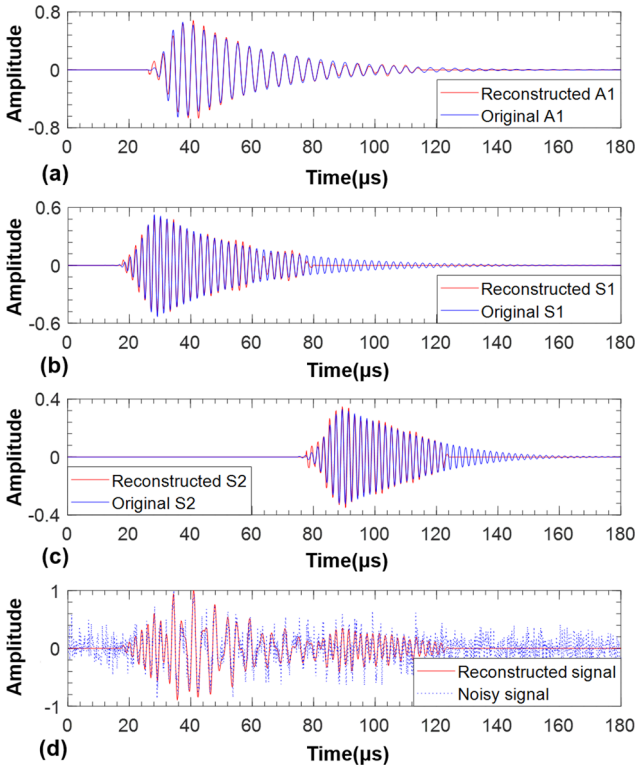

Fig. 4. Reconstructed synthetic signals (SNR = 0 dB): (a) A1 mode; (b) S1 mode; (c) S2 mode; (d) multimode.

with A1 and S1 modes, the extracted S2 signals tends to be slightly different from the original signal because of the lowest waveform amplitude. The result indicates that the proposed method is capable of automatically identifying and reconstructing guided modes.

Fig. 5 illustrates the correlation coefficients between the reconstructed and original signals under varying SNRs. It can be observed that high correlation coefficients can be obtained under the relatively poor SNRs. The correlation coefficients of all modes show a general uptrend with the SNR increasing.

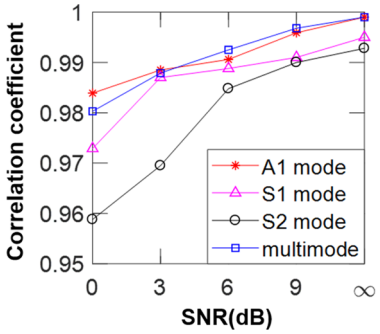

Fig. 5. Correlation coefficients between the reconstructed and original signals with varying SNRs.

4.2. Experimental signals of bovine bone plate and steel plate

4.2.1. Results of bovine bone plate

The mode extraction method was further verified by experimental data recorded on a 4-mm-thick bovine tibia plate with a propagation distance of 70 mm. The SWT representation and the segmentation results of the normalized experimental signal are shown in Fig. 6. The TF energy distribution of the GW signal are in accordance with the theoretical dispersion curves. After SWT representation segmentation, different modes can be identified and separated in the TF domain. Fig. 7d plots the temporal waveform of the measured signal together with its reconstructed result. The reconstructed signal is consistent with the original one with a correlation coefficient of 0.992. Because of low-amplitude, the temporal signal after 120 μs is regarded as noise and filtered out by the algorithm. Fig. 7a–c show the reconstructed experimental signals of A1, S1 and S2 modes, respectively. The TFRs are given in Fig. 8a–c, where the TF energy trajectory of each reconstructed mode is in good agreement with the corresponding theoretical curve.

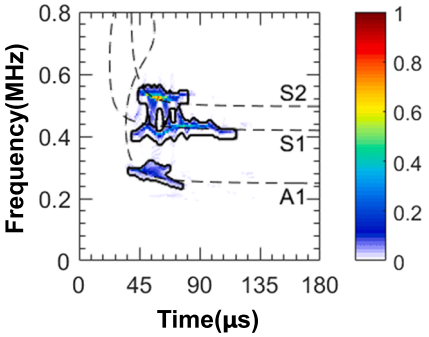

Fig. 6. SWT representation segmentation of the experimental signal measured in the bovine bone plate.

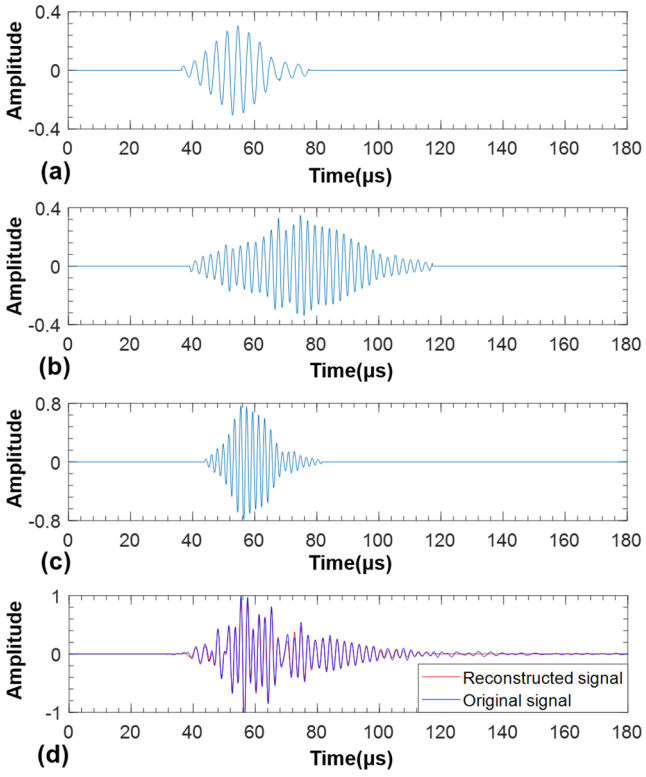

Fig. 7. Reconstructed experimental signals measured in the bovine bone plate: (a) A1 mode; (b) S1 mode; (c) S2 mode; (d) multimode.

4.2.2. Results of steel plate

The experimental signal measured in an 1-mm-thick steel plate [23] was also used to test the method for analyzing ultrasonic GWs signals measured in other waveguides, The SWT representation and modal energy segmentation results are shown in Fig. 9. It is demonstrated that two Lamb modes S0 and A0 can be discriminated clearly in the TF domain. Because of a discontinuity of TFR ridges, A0 mode is separated into two regions on the TF plane, as shown in Fig. 9. The reconstructed temporal waveform is presented in Fig. 10c. The reconstructed signal is similar to the original with a correlation coefficient of 0.932. Fig. 10a and b plot the reconstructed waveforms of S0 and A0 mode, and their corresponding TFRs are given in Fig. 11a and b. It is shown that the TF energy trajectory of each reconstructed mode follows the corresponding theoretical curve.

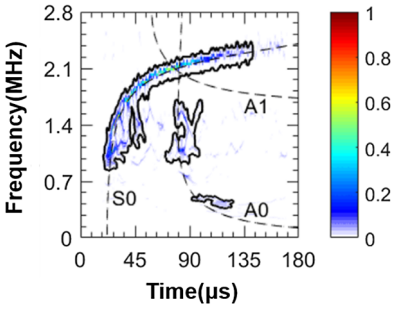

Fig. 9. SWT representation segmentation of the experimental signal measured in the steel plate.

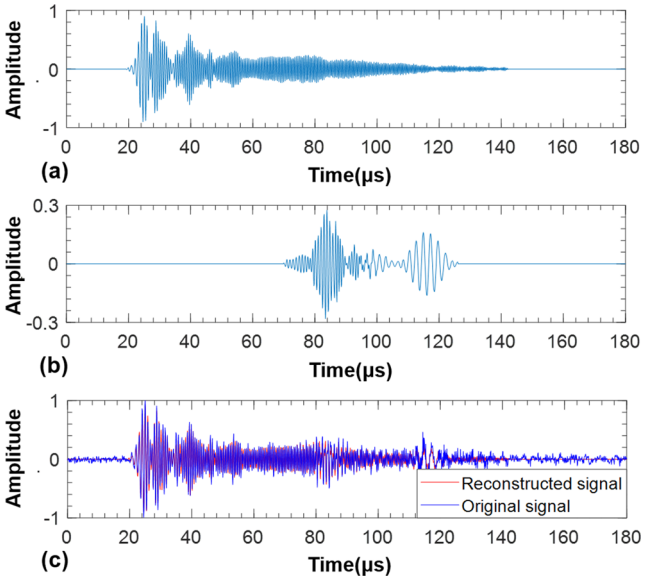

Fig. 10. Reconstructed experimental signals measured in the steel plate: (a) S0 mode; (b) A0 mode; (c) multimode.

5. Discussion

This study proposed an automatic algorithm to separate and reconstruct GW signals transmitted in the plate waveguide. Both synthetic and experimental GWs were used to illustrate the performance of the

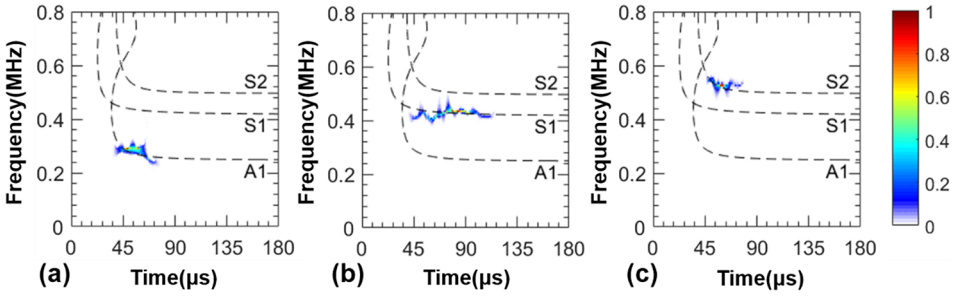

Fig. 8. SWT representation of the reconstructed experimental signal measured in the bovine bone plate: (a) A1 mode; (b) S1 mode; (c) S2 mode.

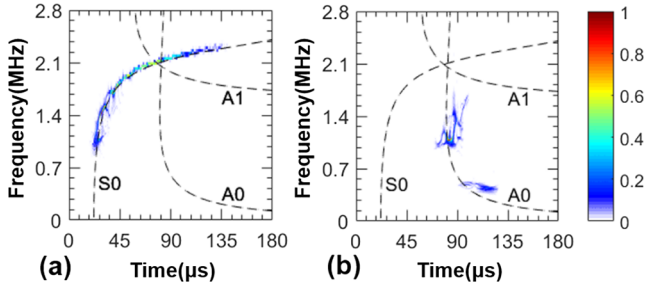

Fig. 11. SWT representation of the reconstructed experimental signal measured in the steel plate: (a) S0 mode; (b) A0 mode.

method. Simulations show that each reconstructed mode is in a good agreement with the original one at different SNRs. The proposed method enables the automatic identification and extraction of individual modes from the synthetic and experimental GWs. The method is suitable to process the ultrasonic GW signals, not only in bone for biomedical application, but also in other waveguides for NDT applications.

For the purpose of mode identification, improvements in TF analysis have been achieved with group delay shift covariant quadratic TFR [41], Chirplet transform [42], matched TFR [43], conjugate time-frequency warping transform [44], frequency-sweep examination method [45] and warblet transform [46]. These methods improve TF resolution and successfully identify mode energy of GW signals in the TF plane, but the time-domain separation was not realized. The proposed method is capable of reconstructing the temporal signals of each individual mode.

There are previous studies of guided mode separation in time domain based on TFR. Xu et al. [47] presented a mode extraction technique using a crazy-climber algorithm. However, due to the complexity of GW dispersion characteristics, manual interaction may be still needed for component identification. Taking the advantage of automatic SWT representation segmentation, our method can separate and reconstruct GW signals without any manual interference. Zhang et al. [36] proposed a joint spectrogram segmentation and ridge-extraction (JSSRE) method to separate different simulated modes based on STFT. Compared with JSSRE, instead of STFT, our method used SWT to enhance the resolution of the TFR. In addition, the SWT-based algorithm presented here was validated by both simulated and experimental signals measured in a long cortical bone and a steel plate.

Some limitations remain in the study. Such a TF-analysis-based mode separation method is developed based on an assumption that the multimodal trajectories are separated in the time-frequency domain. It denotes that the mixed modal energy in a same time-frequency atom cannot be further separated. The proposed method is thus not applicable to extract the individual modes with severe time-frequency overlapping. However, it should be noted that taking the advantage of the high frequency resolution, compared with the conventional TFR methods, such as the STFT, the SWT method shows a better performance for mode identification and component separation. In some previous studies, the mode separations were fulfilled with a consideration of the modal displacement symmetry. For instance, it is possible to separate the fundamental symmetric and asymmetric modes by arranging two receivers on the top and bottom surfaces [48]. The mode orthogonality has been proposed for individual mode extraction [49]. However, with a single channel measurement, it is relatively hard to distinguish the symmetry and antisymmetry of vibration from the corresponding time-frequency trajectory. In future studies, the physical mechanisms could also be considered to improve the GW signal processing.

6. Conclusions

This paper presents a SWT-based mode separation and reconstruction method to extract individual modes from dispersive multimodal GWs. For the simulated signals, all individual modes can be identified and reconstructed with a high accuracy. High correlation coefficients between the original and reconstructed signals under different SNRs confirm the good performance of the proposed method for noise filtering. For the experimental signals, the TFR of each reconstructed mode is consistent with the theoretical dispersion curve. Both simulated and experimental results suggest that the proposed method enables the automatic mode separation of multimodal GWs. This study can be helpful for ultrasonic GW signal processing and nondestructive evaluation.

CRediT authorship contribution statement

Z. Liu: Conceptualization, Data curation, Formal analysis, Writing - original draft, Writing - review & editing. **K. Xu:** Conceptualization, Data curation, Formal analysis, Funding acquisition, Investigation, Methodology, Software, Validation, Visualization, Writing - review & editing. **D. Ta:** Conceptualization, Supervision, Funding acquisition, Investigation, Methodology, Project administration, Resources, Supervision, Validation, Visualization, Writing - review & editing. **D. Li:** Validation, Visualization, Writing - original draft, Writing - review & editing. **W. Wang:** Conceptualization, Supervision, Resources, Writing - original draft, Writing - review & editing.

Acknowledgements

This work was supported by the National Natural Science Foundation (11525416, 11827808 and 11604054), Natural Science Foundation of Shanghai (19ZR1402700), Shanghai Municipal Science and Technology Major Project (2017SHZDZX01) and State Key Laboratory of ASIC and System Project (2018MS004).

Declaration of Competing Interest

All authors state that they have no conflicts of interest.

References

[1] J. Minonzio, N. Bochud, Q. Vallet, Y. Bala, D. Ramiandrisoa, H.E.L.E. Follet, D. Mitton, P. Laugier, Bone cortical thickness and porosity assessment using ultrasound guided waves: an ex vivo validation study, Bone 116 (2018) 111–119.
[2] S.K. Pedram, S. Fateri, L. Gan, A. Haig, K. Thornicroft, Split-spectrum processing technique for SNR enhancement of ultrasonic guided wave, Ultrasonics 83 (2018) 48–59.
[3] Z. Su, L. Ye, Y. Lu, Guided Lamb waves for identification of damage in composite structures: a review, J. Sound Vib. 295 (3–5) (2006) 753–780.
[4] A. Sarvazyan, A. Tatarinov, V. Egorov, S. Airapetian, V. Kurtenok, C.J. Gatt Jr, Application of the dual-frequency ultrasonometer for osteoporosis detection, Ultrasonics 49 (3) (2009) 331–337.
[5] P. Moilanen, A. Salmi, V. Kilappa, Z. Zhao, J. Timonen, E. Hæggström, Phased laser diode array permits selective excitation of ultrasonic guided waves in coated bone-mimicking tubes, J. Appl. Phys. 122 (14) (2017) 144901.
[6] X. Song, D. Ta, W. Wang, Analysis of superimposed ultrasonic guided waves in long bones by the joint approximate diagonalization of eigen-matrices algorithm, Ultrasound Med. Biol. 37 (10) (2011) 1704–1713.
[7] S. Grondel, C. Paget, C. Delebarre, J. Assaad, K. Levin, Design of optimal configuration for generating A0 Lamb mode in a composite plate using piezoceramic transducers, J. Acoust. Soc. Am. 112 (1) (2002) 84–90.
[8] L. Bai, K. Xu, N. Bochud, D. Ta, B. Hu, P. Laugier, J. Minonzio, Multichannel wideband mode-selective excitation of ultrasonic guided waves in long cortical bone, 2016 IEEE International Ultrasonics Symposium (IUS), 2016, pp. 1–4.
[9] G.A. McMechan, M.J. Yedlin, Analysis of dispersive waves by wave field transformation, Geophysics 46 (6) (1981) 869–874.
[10] J. Minonzio, M. Talmant, P. Laugier, Guided wave phase velocity measurement using multi-emitter and multi-receiver arrays in the axial transmission configuration, J. Acoust. Soc. Am. 127 (5) (2010) 2913–2919.
[11] K. Kassou, Y. Remram, P. Laugier, J. Minonzio, dispersion characteristics of the flexural wave assessed using low frequency (50–150 kHz) point-contact transducers: a feasibility study on bone-mimicking phantoms, Ultrasonics 81 (2017) 1–9.

[12] J.B. Harley, J.M. Moura, Sparse recovery of the multimodal and dispersive characteristics of Lamb waves, J. Acoust. Soc. Am. 133 (5) (2013) 2732–2745.
[13] W. Zhao, M. Li, J.B. Harley, Y. Jin, J.E.M. Moura, J. Zhu, Reconstruction of Lamb wave dispersion curves by sparse representation with continuity constraints, J. Acoust. Soc. Am. 141 (2) (2017) 749–763.
[14] F. Gao, L. Zeng, J. Lin, Z. Luo, Mode separation in frequency–wavenumber domain through compressed sensing of far-field Lamb waves, Meas. Sci. Technol. 28 (7) (2017) 75004.
[15] A. Drémeau, F.L. Courtois, J. Bonnel, Reconstruction of dispersion curves in the frequency-wavenumber domain using compressed sensing on a random array, IEEE J. Oceanic Eng. 42 (4) (2017) 914–922.
[16] K. Xu, J. Minonzio, D. Ta, B. Hu, W. Wang, P. Laugier, Sparse SVD method for high-resolution extraction of the dispersion curves of ultrasonic guided waves, IEEE Trans. Ultrason. Ferroelectr. Freq. Control 63 (10) (2016) 1514–1524.
[17] S. Okumura, V. Nguyen, H. Taki, G. Haïat, S. Naili, T. Sato, Rapid high-resolution wavenumber extraction from ultrasonic guided waves using adaptive array signal processing, Appl. Sci. 8 (4) (2018) 2076–3417.
[18] G. Beylkin, Discrete radon transform, IEEE Trans. Acoust. Speech Signal Process. 35 (2) (1987) 162–172.
[19] Y. Luo, J. Xia, R.D. Miller, Y. Xu, J. Liu, Q. Liu, Rayleigh-wave dispersive energy imaging using a high-resolution linear Radon transform, Pure Appl. Geophys. 165 (5) (2008) 903–922.
[20] T.N. Tran, L.H. Le, M.D. Sacchi, V. Nguyen, E.H. Lou, Multichannel filtering and reconstruction of ultrasonic guided wave fields using time intercept-slowness transform, J. Acoust. Soc. Am. 136 (1) (2014) 248–259.
[21] K. Xu, D. Ta, D. Cassereau, B. Hu, W. Wang, P. Laugier, J. Minonzio, Multichannel processing for dispersion curves extraction of ultrasonic axial-transmission signals: comparisons and case studies, J. Acoust. Soc. Am. 140 (3) (2016) 1758–1770.
[22] K. Xu, P. Laugier, J. Minonzio, Dispersive Radon transform, J. Acoust. Soc. Am. 143 (5) (2018) 2729–2743.
[23] K. Xu, D. Ta, P. Moilanen, W. Wang, Mode separation of Lamb waves based on dispersion compensation method, J. Acoust. Soc. Am. 131 (4) (2012) 2714–2722.
[24] M. Zhao, L. Zeng, J. Lin, W. Wu, Mode identification and extraction of broadband ultrasonic guided waves, Meas. Sci. Technol. 25 (11) (2014) 115005.
[25] F. Auger, P. Flandrin, Y. Lin, S. McLaughlin, S. Meignen, T. Oberlin, H. Wu, Time-frequency reassignment and synchrosqueezing: an overview, IEEE Signal Process Mag. 30 (6) (2013) 32–41.
[26] S. Wang, S. Huang, Q. Wang, Y. Zhang, W. Zhao, Mode identification of broadband Lamb wave signal with squeezed wavelet transform, Appl. Acoust. 125 (2017) 91–101.
[27] I. Daubechies, A nonlinear squeezing of the continuous wavelet transform based on auditory nerve models, Wavel. Med. Biol. (1996) 527–546.
[28] G. Thakur, E. Brevdo, N.S. Fučkar, H. Wu, The synchrosqueezing algorithm for time-varying spectral analysis: robustness properties and new paleoclimate applications, Signal Process. 93 (5) (2013) 1079–1094.
[29] R.H. Herrera, J. Han, M. van der Baan, Applications of the synchrosqueezing transform in seismic time-frequency analysis, Geophysics 79 (3) (2014) V55–V64.
[30] J.P. Amezquita-Sanchez, H. Adeli, Synchrosqueezed wavelet transform-fractality model for locating, detecting, and quantifying damage in smart highrise building structures, Smart Mater. Struct. 24 (6) (2015) 65034.
[31] M. Clausel, T. Oberlin, V. Perrier, The monogenic synchrosqueezed wavelet transform: a tool for the decomposition/demodulation of AM–FM images, Appl. Comput. Harmon. Anal. 39 (3) (2015) 450–486.
[32] F. Bause, B. Henning, B. Huang, A. Kunoth, Ultrasonic waveguide signal decomposition using the synchrosqueezed wavelet transform for modal group delay computation, 2013 IEEE International Ultrasonics Symposium (IUS), 2013, pp. 671–674.
[33] J. Ikram, A. Papandreou-Suppappola, G. Li, and A. Chattopadhyay, Guided wave based inspection of integrated circuit packages using the time-frequency synchrosqueezing transform, in Smart Structures and NDE for Energy Systems and Industry 4.0, 2019, 109730A.
[34] J.B. Roerdink, A. Meijster, The watershed transform: definitions, algorithms and parallelization strategies, Fundamenta Informaticae 41 (1, 2) (2000) 187–228.
[35] J. Fan, D.K. Yau, A.K. Elmagarmid, W.G. Aref, Automatic image segmentation by integrating color-edge extraction and seeded region growing, IEEE Trans. Image Process. 10 (10) (2001) 1454–1466.
[36] Z. Zhang, K. Xu, D. Ta, W. Wang, Joint spectrogram segmentation and ridge-extraction method for separating multimodal guided waves in long bones, Sci. China Phys., Mech. Astron. 56 (7) (2013) 1317–1323.
[37] K. Xu, D. Ta, B. Hu, P. Laugier, W. Wang, Wideband dispersion reversal of Lamb waves, IEEE Trans. Ultrason. Ferroelectr. Freq. Control 61 (6) (2014) 997–1005.
[38] F. Meyer, Topographic distance and watershed lines, Signal Process. 38 (1) (1994) 113–125.
[39] Q. Jiang, B.W. Suter, Instantaneous frequency estimation based on synchrosqueezing wavelet transform, Signal Process. 138 (2017) 167–181.
[40] S. Chen, R.M. Haralick, Recursive erosion, dilation, opening, and closing transforms, IEEE Trans. Image Process. 4 (3) (1995) 335–345.
[41] A. Papandreou-Suppappola, R.L. Murray, B. Iem, G.F. Boudreaux-Bartels, Group delay shift covariant quadratic time-frequency representations, IEEE Trans. Signal Process. 49 (11) (2001) 2549–2564.
[42] H. Kuttig, M. Niethammer, S. Hurlebaus, L.J. Jacobs, Model-based analysis of dispersion curves using chirplets, J. Acoust. Soc. Am. 119 (4) (2006) 2122–2130.
[43] G. Le Touzé, B. Nicolas, J.L. Mars, J. Lacoume, Matched representations and filters for guided waves, IEEE Trans. Signal Process. 57 (5) (2009) 1783–1795.
[44] J. Bonnel, B. Nicolas, J.I. Mars, S.C. Walker, Estimation of modal group velocities with a single receiver for geoacoustic inversion in shallow water, J. Acoust. Soc. Am. 128 (2) (2010) 719–727.
[45] S. Fateri, N.V. Boulgouris, A. Wilkinson, W. Balachandran, T. Gan, Frequency-sweep examination for wave mode identification in multimodal ultrasonic guided wave signal, IEEE Trans. Ultrason. Ferroelectr. Freq. Control 9 (61) (2014) 1515–1524.
[46] Y. Yang, Z.K. Peng, W.M. Zhang, G. Meng, Z.Q. Lang, Dispersion analysis for broadband guided wave using generalized warblet transform, J. Sound Vib. 367 (2016) 22–36.
[47] K. Xu, D. Ta, W. Wang, Multiridge-based analysis for separating individual modes from multimodal guided wave signals in long bones, IEEE Trans. Ultrason. Ferroelectr. Freq. Control 57 (11) (2010) 2480–2490.
[48] F. Benmeddour, S.E.B. Grondel, J. Assaad, E. Moulin, Study of the fundamental Lamb modes interaction with symmetrical notches, NDT and E Int. 41 (1) (2008) 1–9.
[49] M. Ratassepp, Z. Fan, K. Lasn, Wave mode extraction from multimodal wave signals in an orthotropic composite plate, Ultrasonics 71 (2016) 223–230.